Anti-$\mathcal{PT}$ symmetry in dissipatively coupled optical systems

Fan Yang,[1] Yong-Chun Liu,[1,2,*] and Li You[1,2,†]

[1]*State Key Laboratory of Low-Dimensional Quantum Physics, Department of Physics, Tsinghua University, Beijing 100084, China*

[2]*Collaborative Innovation Center of Quantum Matter, Beijing 100084, China*

(Received 3 May 2017; published 21 November 2017)

We show that anti-$\mathcal{PT}$ symmetry can be realized in dissipatively coupled optical systems. Its emergence gives rise to spontaneous phase transitions for the guided and localized photonic eigenmodes in the waveguide and cavity systems studied, respectively. As a ubiquitous feature we demonstrate that constant refraction [analogous to unit refraction in [Nat. Phys. **12**, 1139 (2016)]] occurs in the $\mathcal{PT}$-symmetric phase, which leads to several interesting properties for the photonic system, such as flat broadband light transport and dispersion-induced dissipation.

DOI: 10.1103/PhysRevA.96.053845

I. INTRODUCTION

A non-Hermitian Hamiltonian H can exhibit physics beyond that of a closed system [1–6]. As a striking example, parity-time ($\mathcal{PT}$) symmetry, defined by $[\mathcal{PT}, H] = 0$ and proposed by Bender and Boettcher [1], has drawn much attention in recent years [6–18]. Such a system can possess entirely real-valued eigenenergy spectra below the symmetry-breaking threshold.

Optical systems provide ideal platforms for studying non-Hermitian physics, because tunable complex potentials for photons can be constructed by easily incorporating gain or loss. The realization of $\mathcal{PT}$ symmetry in photonic systems [8,13,15] not only advances the study of non-Hermitian physics but also leads to unprecedented properties in photonics, ranging from the asymmetric light transport [8,11], simultaneous coherent perfect absorption and lasing [9,10], etc. in earlier studies, to the superprism effect [19] and enhanced metrological precision [20] in more recent investigations. In addition to gain-loss systems, the $\mathcal{PT}$ phase transition can also be measured in topological photonic systems [21] and complex-frequency band structures [22].

Anti-$\mathcal{PT}$ symmetry, with the commutator replaced by the anticommutator, or $\{\mathcal{PT}, H\} = 0$, represents a generalization of $\mathcal{PT}$ symmetry. Systems with anti-$\mathcal{PT}$ symmetry can display distinct intriguing properties in the absence of any gain medium [23–26]. The original proposal treated anti-$\mathcal{PT}$ symmetry by assuming a balanced positive and negative refraction [23]. Subsequent theoretical studies were based on cold-atom lattices [24] and nonlinear optical systems [25]. The first experiment reported recently employed dissipative couplings between atomic spin waves from atoms in transport [26].

For real applications, an implementation of anti-$\mathcal{PT}$ symmetry in an integrable and tunable linear photonic system is highly desired. This paper presents an easy-to-implement scheme for realizing anti-$\mathcal{PT}$ symmetry in practical photonic systems, e.g., solid-state linear optical waveguides or optical cavity configurations. Our proposal illuminates the paradigm feature of the anti-Hermitian Hamiltonian with indirect dissipative coupling. Unlike Hermitian couplings that balance the gain and loss in $\mathcal{PT}$-symmetric systems [8,15], anti-Hermitian couplings are exploited here to balance the detuning between photonic modes. The resulting anti-$\mathcal{PT}$ symmetry causes a spontaneous phase transition of the eigenstates (characterized by $\mathcal{PT}$ symmetry breaking), which significantly influences the eigenvalues as well as the transport properties. The consequent constant-refraction in the symmetry unbroken regime gives rise to several interesting phenomena, such as detuning-induced attenuation, which transfers a pure dispersion modulation into a pure dissipation modulation and enables controlling of the loss rate for an open system.

II. COUPLED WAVEGUIDE SYSTEM

For light propagation along the z direction in a system consisting of three waveguides as shown in Fig. 1(a), the total field is expanded as $\mathbf{E}(\mathbf{r}) = a(z)\mathbf{E}_a(x,y) + b(z)\mathbf{E}_b(x,y) + c(z)\mathbf{E}_c(x,y)$, with the guided modes denoted by $m = a$, b, and c, respectively. The mode function $\mathbf{E}_m(x,y)$ for the field distribution is normalized such that $|a(z)|^2$, $|b(z)|^2$, and $|c(z)|^2$ correspond to photon number flux carried by the corresponding mode [27]. Modes a and b are coupled to the mode c through near-field tunneling [8,28], while a and b are not directly coupled. The system is described by the model Hamiltonian $H_c = \kappa_1 a^\dagger c + \kappa_2 b^\dagger c + \text{H.c.}$, where κ_1 and κ_2 represent the hopping rate between mode a and c, and the hopping rate between mode b and c, respectively. These hopping rates can be rigorously calculated via the overlap integral between the mode field distribution functions [28]. All mode annihilation operators a, b, and c will be treated approximately as c-numbers in the classical limit, with their associated quantum noises neglected.

When mode c is lossy with an attenuation rate $\gamma \gg \kappa_{1/2}$, it can be adiabatically eliminated (see Appendix A). For balanced coupling ($\kappa_2 \approx \kappa_1 = \kappa$) and when the propagation constant detuning Δk_1 (Δk_2) between mode c and mode a (b) is small enough ($|\Delta k_1|, |\Delta k_2| \ll \gamma$), the effective coupling Hamiltonian reduces to $H_c = i\Gamma(a^\dagger b + b^\dagger a)$, with the effective "dissipative" coupling rate $\Gamma = |\kappa|^2/\gamma$. Interestingly, H_c is anti-Hermitian ($H_c^\dagger = -H_c$), which plays a key role in our implementation of anti-$\mathcal{PT}$ symmetry.

Using a vector $\Psi = e^{i\bar{k}z}(a,b)^T$ to describe the state of the system with $\bar{k} = (k_a' + k_b')/2$ and k_a' and k_b' the modified propagation constants for the two respective modes, the equivalent Schrödinger-like equation is given by (see Appendix A)

$$i\partial_z \Psi = H\Psi, \tag{1}$$

*ycliu@mail.tsinghua.edu.cn

†lyou@mail.tsinghua.edu.cn

with the effective Hamiltonian

$$H = \begin{pmatrix} \Delta - i\Gamma & -i\Gamma \\ -i\Gamma & -\Delta - i\Gamma \end{pmatrix}, \tag{2}$$

and $\Delta = (k_a - k_b)/2$ is the effective detuning. For the waveguide model system, the time-reversal operation $\mathcal{T}$ transforms a z-independent operator to its complex conjugate, while the parity operator $\mathcal{P}$ exchanges locations of the modes [7,8]. Thus, it is easy to verify that our model Hamiltonian Eq. (2) is anti-$\mathcal{PT}$-symmetric, i.e.,

$$(\mathcal{PT})H(\mathcal{PT})^{-1} = \mathcal{P}H^*\mathcal{P}^{-1} = -H. \tag{3}$$

We now discuss the spontaneous phase transition of the above model. Denoting its eigenstate as $\Psi_\pm = (a_\pm, b_\pm)^T$ with corresponding eigenvalue $\beta_\pm$, we can easily obtain $H(\mathcal{PT}\Psi_\pm) = -\beta_\pm^*(\mathcal{PT}\Psi_\pm)$ by using Eq. (3), which gives the following two possibilities: (i) $\beta_\pm$ is pure imaginary and $\mathcal{PT}\Psi_\pm = \sigma_\pm\Psi_\pm$ with $|\sigma_\pm|^2 = 1$; (ii) $\beta_\pm^* = -\beta_\mp$ and $\mathcal{PT}\Psi_\pm = \sigma_\pm\Psi_\mp$ with $\sigma_\pm^*\sigma_\mp = 1$. They correspond to the two different phases: the $\mathcal{PT}$-symmetric phase (i), where each eigenstate is also an eigenstate of the $\mathcal{PT}$ operator and thus possesses the same level of symmetry as the Hamiltonian; and the symmetry-broken phase (ii), where the $\mathcal{PT}$ operation transforms one eigenvector into the other, and neither eigenstates are $\mathcal{PT}$-symmetric themselves. The analytical eigensolutions of the model Hamiltonian (2) show that the system lies in the $\mathcal{PT}$-symmetric phase with eigenvalues $\beta_\pm = -i[\Gamma \pm (\Gamma^2 - \Delta^2)^{1/2}]$ when the dissipative coupling $\Gamma > \Delta$ (for $\Delta > 0$). The corresponding eigenvectors are $\Psi_\pm = (\pm e^{\pm i\phi}, 1)^T$ with $\sin\phi = \Delta/\Gamma$. In this phase, the two eigenmodes share identically the same real propagation constant (constant-refraction effect) but with different attenuation rates, and both modes exhibit balanced field profiles since $|a_\pm/b_\pm| = 1$. As the coupling-to-detuning ratio (Γ/Δ) decreases, the system remains in the symmetric phase until $\Gamma = \Delta$, the exceptional point (EP), at which the two eigenmodes coalesce into a degenerate one. When $\Gamma < \Delta$, the system undergoes a transition into the symmetry-broken phase with $\beta_\pm = -i\Gamma \pm (\Delta^2 - \Gamma^2)^{1/2}$ and $\Psi_\pm = (ie^{\pm r}, 1)^T$ $(\cosh r = \Delta/\Gamma)$, where the two eigenmodes decay with the same rate but propagate with different wave vectors and exhibit an asymmetric field distribution $|a_+/b_+| = |b_-/a_-| > 1$.

This phase transition is illustrated for the two-dimensional (2D) planar waveguide system shown in Fig. 1(b) in terms of its fundamental transverse electric mode. The effective index n_{eff} and the amplitude ratio $|a_\pm/b_\pm|$ of the eigenmode versus Γ/Δ are presented in Figs. 1(c)–1(e), which show clearly that the ratio of Γ/Δ explicitly distinguishes the two phases. In addition, the analytical results agrees well with the finite element method (FEM) simulations.

The phase transition discussed above can significantly modify the transport properties of our system, whose evolution is characterized by the operator $U(z) = e^{-iHz}$. In the symmetric phase, we find

$$U = e^{-\Gamma z}\begin{pmatrix} \cosh sz - i\frac{\Delta}{s}\sinh sz & -\frac{\Gamma}{s}\sinh sz \\ -\frac{\Gamma}{s}\sinh sz & \cosh sz + i\frac{\Delta}{s}\sinh sz \end{pmatrix}, \tag{4}$$

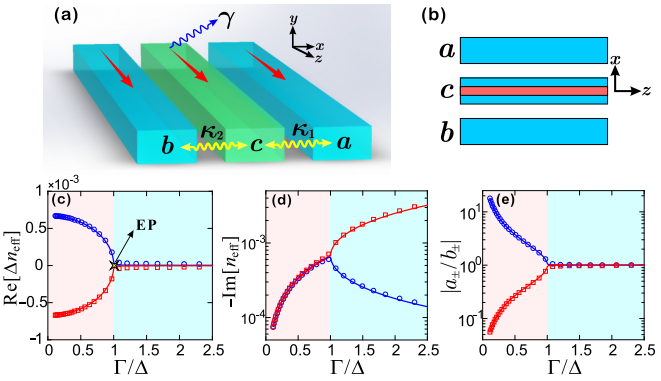

FIG. 1. (a) The coupled waveguide schematics for implementing anti-$\mathcal{PT}$ symmetry. (b) Its structure illustration for the planar waveguide system. The width of each waveguide is $0.3\lambda_0$. The refractive index is $3.5 - 0.12i$ for the inner one third of waveguide c (red region), while it is fixed at 3.5 for waveguide b and the rest of waveguide c, and is adjustable for waveguide a (denoted by n_a). (c), (d) Characteristics of the eigen-waveguide modes of the structure shown in (b) with $n_a = 3.5013$. Γ/Δ is varied by changing the distance d between the adjacent waveguides from $0.12\lambda_0$ to $0.2\lambda_0$. The circles and squares are obtained by FEM simulations, and the solid lines are obtained with the analytical theory.

with $s = (\Gamma^2 - \Delta^2)^{1/2}$, and in the symmetry-broken phase

$$U = e^{-\Gamma z}\begin{pmatrix} \cos qz - i\frac{\Delta}{q}\sin qz & -\frac{\Gamma}{q}\sin qz \\ -\frac{\Gamma}{q}\sin qz & \cos qz + i\frac{\Delta}{q}\sin qz \end{pmatrix}, \tag{5}$$

with $q = (\Delta^2 - \Gamma^2)^{1/2}$. In the $\mathcal{PT}$-symmetric phase according to Eq. (4), the state evolves as hyperbolic functions and exhibits no interference fringes along the z direction. While for the symmetry-broken phase [Eq. (5)], oscillations of the mode amplitudes occur along the propagation direction. Such a contrasting difference can be observed with a setup of the initial incidence from mode a. We find that, from Eqs. (4) and (5), the splitting ratio $|b/a|^2$ in the two phases becomes

$$\left|\frac{b}{a}\right|^2 = \begin{cases} \dfrac{\Gamma^2}{s^2\coth^2 sz + \Delta^2} & (\Gamma > \Delta) \\ \dfrac{\Gamma^2}{q^2\cot^2 qz + \Delta^2} & (\Gamma < \Delta), \end{cases} \tag{6}$$

exhibiting completely different transport properties. In the $\mathcal{PT}$-symmetric phase, the energy of mode a gradually flows to mode b and the splitting ratio always converges to unity [see Fig. 2(a)]. In this case, the anti-Hermitian couplings can balance the wave-vector detuning between modes a and b and filter out the high-loss eigenmode after propagation. Further increase of the detuning breaks this balance and brings the system to the symmetry-broken regime, where energy cyclically flows back and forth between the two modes [see Fig. 2(b)], facilitated by the interference of the eigenmodes with the same loss rate but different wave vectors.

The unique transport property in the $\mathcal{PT}$-symmetric phase promises several interesting applications. When $\Delta = 0$, the system supports a very lossy symmetric eigenmode $\Psi_s = (1,1)^T/\sqrt{2}$ (loss rate being 2Γ), and a lossless antisymmetric mode $\Psi_a = (1,-1)^T/\sqrt{2}$. Thus, the symmetric mode can be

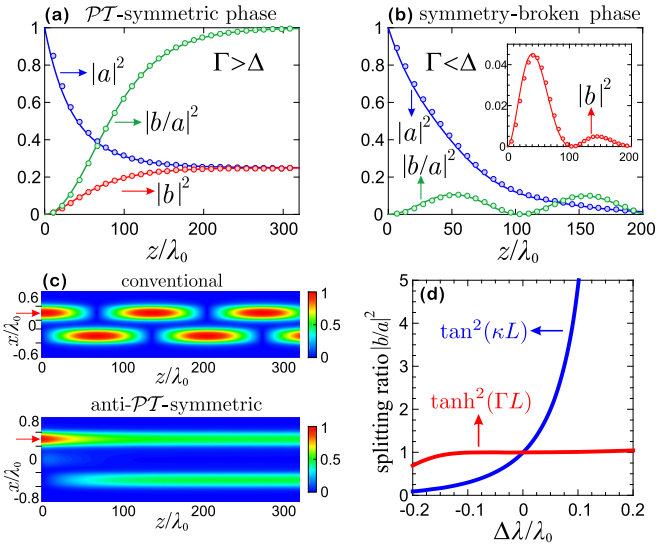

FIG. 2. Characteristics of the state evolution in the structure shown in Fig. 1(b) for $d = 0.12\ \lambda_0$. Panels (a) and (b) show the transport properties in the $\mathcal{PT}$-symmetric phase ($n_a = 3.5$, $\Delta = 0$) and the symmetry-broken phase ($n_a = 3.51$, $\Gamma/\Delta = 0.3458$), respectively. Circles are obtained by FEM and the solid lines are based on the analytical model. Panels (c) and (d) show the FEM simulations for a conventional DC ($d = 0.17\ \lambda_0$) and the system considered in panel (a). (c) Electric-field distributions [$|\mathbf{E}(x,z)|$]. (d) Splitting-ratio spectrum for a conventional DC [blue (steeper) curves, $L = 20.8\ \lambda_0$] and an anti-$\mathcal{PT}$-symmetric system [red (flatter) curves, $L = 300\ \lambda_0$]. $\Delta\lambda$ denotes the deviation from the center wavelength (at which $|b/a|^2 = 1$).

filtered after a sufficient propagation length L, which can be used to construct a mode filter as well as a 3dB splitter [by sacrificing half of the total energy carried by the lossy mode to make $|b/a|^2 = \tanh^2(\Gamma L) \approx 1$]. This transport behavior differs from that in a conventional directional coupler (DC) or a multimode interference (MMI) device [29], which relies on the interference of the propagating modes and shows a strong dependence on frequency and coupling length. For example, a DC with a Hermitian coupling strength κ gives $|b/a|^2 = \tan^2(\kappa L)$ [28]. This difference is shown in Figs. 2(c) and 2(d), which clearly illustrates the featured constant-refraction and flat broadband transport of an anti-$\mathcal{PT}$-symmetric system. Such a 3dB splitting is also robust against variations of the detuning Δ.

A second rather counterintuitive feature is detuning-induced attenuation. For an input field in the antisymmetric mode Ψ_a, the transmission coefficients for the symmetric and antisymmetric modes are given by $t_a = \Psi_a^\dagger U(z)\Psi_a$ and $t_s = \Psi_s^\dagger U(z)\Psi_a$, respectively, after propagating through the system. For a large optical depth $\alpha = \Gamma z$ ($e^{-\alpha} \ll 1$), we obtain $|t_a|^2 \approx e^{-\alpha(\Delta/\Gamma)^2}$ and $|t_s|^2 \ll 1$ in the $\mathcal{PT}$-symmetric phase. This indicates that we can turn a refractive index modulation to a pure absorption modulation, e.g., when the refractive index of one waveguide is tuned away from the other one, the transmittance of the antisymmetric mode can be changed from unity to a rather small value while the excitation of the symmetric mode remains negligible (see Fig. 3). The change of the refractive index here does not cause

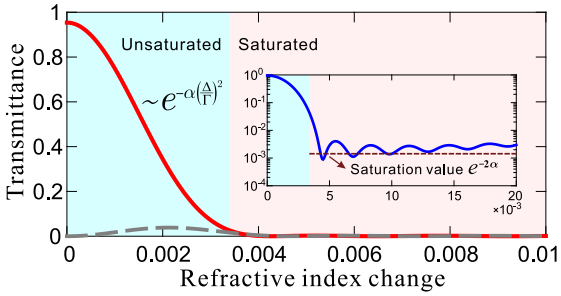

FIG. 3. The dependence of transmittance for the antisymmetric mode ($|t_a|^2$, red solid curve) and the symmetric mode ($|t_s|^2$, gray dashed curve) on the change of the refractive index of waveguide a (defined as $n_a - 3.5$) with an optical depth $\alpha \approx 3.3$. The inset shows the total transmittance ($|t_a|^2 + |t_s|^2$, blue solid curve) and the saturation value (brown dashed curve).

additional refraction as one would expect in a conventional Mach–Zehnder (MZ) modulator, where the index modulation induces an oscillation of $|t_a|^2$ and $|t_s|^2$. However, entering the symmetry-broken phase, this absorption modulation gradually becomes "saturated", i.e., further increase of the detuning does not continuously increase the attenuation, the transmittance $|t_a|^2$ as well as $|t_s|^2$ begins to oscillate with $|t_a|^2 + |t_s|^2$ converging to $e^{-2\alpha}$ (see the inset of Fig. 3).

III. MICROCAVITY REALIZATION

To facilitate anti-$\mathcal{PT}$ symmetry in the time domain and its associated resonance effect, we consider a second realization with optical cavity configurations, based on ring cavities side coupled to waveguides. The anti-$\mathcal{PT}$ symmetry can be implemented by an auxiliary lossy cavity with mode c to form an effective dissipative coupling between modes a and b [referred to as Config. 1; see Fig. 4(a)], in the same manner as the waveguide system. Alternatively, the same dissipative couplings can be obtained by connecting two separated cavities with two common waveguides as shown in Fig. 4(b) (referred to as Config. 2). In this latter case, the effective couplings can be continuously tuned from Hermitian to anti-Hermitian [30]. The equation of motion for both configurations takes the form

$$i\,\partial_t \Psi = H\Psi + \mathcal{D}, \tag{7}$$

where $\Psi = e^{i\bar{\omega}t}(a,b)^T$ represents the amplitudes of the two cavity modes with $\bar{\omega}$ being the average resonance frequency for modes a and b, $\mathcal{D}$ denoting a driving term, and the effective Hamiltonian being given by

$$H = \begin{pmatrix} \Delta - i\gamma' & -i\Gamma \\ -i\Gamma & -\Delta - i\gamma' \end{pmatrix}, \tag{8}$$

with $\Delta = (\omega_a - \omega_b)/2$. For Config. 1, the parameters are $\Gamma = 2\kappa^2/\gamma$ and $\gamma' = \Gamma + (\gamma_0 + \gamma_i)/2$, where γ_i denotes the same intrinsic decay rate of mode a and b. In Config. 2, they are $\Gamma = \gamma_0 u$ and $\gamma' = \gamma_0 + \gamma_i/2$, where $u = e^{i\theta}$ is the propagation phase factor in the common waveguide and can be treated as frequency independent within the spectra of interest. The anti-Hermitian coupling requires $u = \pm 1$ and we choose $u = 1$ here.

The anti-$\mathcal{PT}$-symmetric Hamiltonian (10) gives rise to a spontaneous phase transition for the eigencavity modes as well.

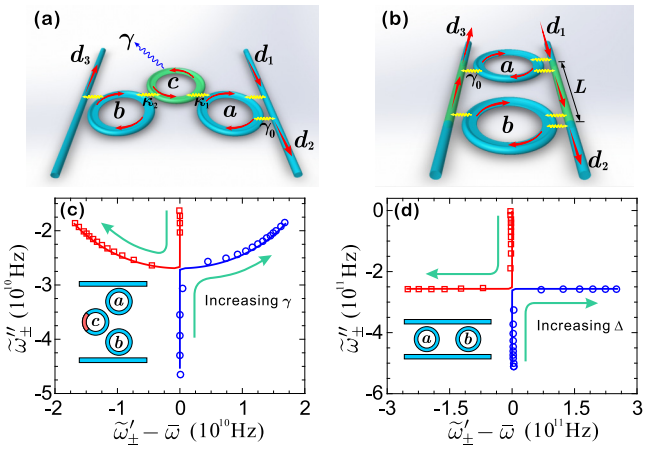

FIG. 4. The coupled cavities schematics of (a) Config. 1 and (b) Config. 2. Panels (c) and (d) show the evolution of the eigenfrequencies in the complex plane for Config. 1 and Config. 2, respectively. The circles and the solid lines are obtained respectively by FEM and the coupled mode model for the corresponding 2D structures sketched in the insets. The refractive index of the material is 3.5. In Config. 1, a quarter of cavity c is modulated to have a varying imaginary refractive index (from 0.031 to 0.06) which changes γ. In Config. 2, the tuning of Δ is achieved by changing the inner radius of the cavity b. The detailed structure parameters are given in Appendix B.

In the $\mathcal{PT}$-symmetric phase ($\Gamma > \Delta$), the eigenmodes take the same resonance frequency but different decay rates. For $\Gamma < \Delta$, the symmetry-broken eigenmodes take nondegenerate resonance frequencies but exhibit the same decay rate. The numerical verifications are shown in Figs. 4(c) and 4(d). In Fig. 4(c), we consider Config. 1. As the decay rate of mode c changes, the coupling rate Γ continuously varies, and the evolution of the eigenfrequency $\tilde{\omega}_\pm = \tilde{\omega}'_\pm + i\tilde{\omega}''_\pm$ displays different trends before and after the EP ($\Gamma = \Delta$). The reversed evolution of the decay rate for one of the eigenmodes (red curve) leads to loss-induced suppression and revival of lasing, accompanied by a reversed trajectory to that of the $\mathcal{PT}$-symmetric Hamiltonian [31]. The dependence of the eigenfrequency of Config. 2 on the detuning Δ is presented in Fig. 4(d). In the $\mathcal{PT}$-symmetric phase, increase of the detuning does not split the resonance frequency of the two eigenmodes but can significantly modulate the decay rates of these modes. This effect can be used to turn a dispersive modulation to a pure dissipative modulation of the cavity modes, with the latter being crucial for some novel modulation schemes [32]. In the symmetry-broken phase, the dissipative coupling cannot balance the large detuning, and the dispersive modulation returns to its original role. Such dispersion-induced dissipation effects do not appear in an ordinary non-Hermitian system, where dispersive variation always simultaneously changes refraction and loss.

Figure 5 shows the field distributions for the eigenmodes of Config. 2. When $\Gamma > \Delta$, one dark mode [Fig. 5(a)] and one bright mode [Fig. 5(b)] with the same resonance frequency are formed due to the preserved $\mathcal{PT}$ symmetry. The existence of such a mode pair makes this system capable of implementing the optical analogy of electromagnetically induced

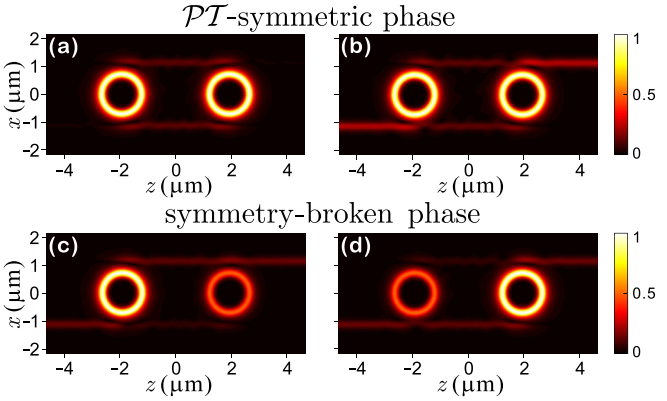

FIG. 5. Field distributions of the eigenmodes for Config. 2. Panels (a) and (b) show the two modes in the $\mathcal{PT}$-symmetric phase with $\Gamma/\Delta = 6.696$, while panels (c) and (d) are for the symmetry-broken phase with $\Gamma/\Delta = 0.79$.

transparency (EIT) [33–36]. When $\Gamma < \Delta$, the symmetry is broken, and the two eigenmodes take the same coupling loss but exhibit asymmetric field distributions [Figs. 5(c) and 5(d)].

To enhance the resolution of the EP, we propose to probe the resonance structure by a time-domain measurement. We consider the dynamical evolution of a short pulse in the anti-$\mathcal{PT}$-symmetric cavity system shown in Fig. 4(b). The following analysis, however, is more general and is not limited to this structure.

Transforming the equation of motion to the frame rotating with the carrier frequency ω_0 of the incident pulse $d_1(t) = \tilde{d}_1(t)e^{-i\omega_0 t}$, we obtain

$$i\frac{d}{dt}\begin{pmatrix}\tilde{a}\\ \tilde{b}\end{pmatrix} = \begin{pmatrix}\Delta - \delta - i(\gamma_i/2+\gamma_0) & -iu\gamma_0\\ -iu\gamma_0 & -\Delta-\delta-i(\gamma_i/2+\gamma_0)\end{pmatrix} \times\begin{pmatrix}\tilde{a}\\ \tilde{b}\end{pmatrix} - i\sqrt{\gamma_0}\begin{pmatrix}\tilde{d}_1\\ u\tilde{d}_1\end{pmatrix}, \tag{9}$$

where $\tilde{a}(t) = a(t)e^{i\omega_0 t}$, $\tilde{b}(t) = b(t)e^{i\omega_0 t}$ are the slowly varying mode amplitudes, $\Delta = (\omega_a - \omega_b)/2$ is the effective detuning of the two cavities (assuming $\Delta > 0$), and $\delta = \omega_0 - \bar{\omega}$ is set to be zero. With the input-output relations [37], the transmitted amplitude $\tilde{d}_2(t)$ and the reflected amplitude $\tilde{d}_3(t)$ are determined by

$$\tilde{d}_2 = u\tilde{d}_1 + u\sqrt{\gamma_0}\tilde{a} + \sqrt{\gamma_0}\tilde{b}, \tag{10}$$

$$\tilde{d}_3 = u\sqrt{\gamma_0}\tilde{b} + \sqrt{\gamma_0}\tilde{a}. \tag{11}$$

To obtain the anti-$\mathcal{PT}$-symmetric Hamiltonian, we choose $u = 1$, $\Gamma = \gamma_0$. Then, by applying a Fourier transform to Eq. (9) [e.g., $\tilde{a}[\omega] = \frac{1}{\sqrt{2\pi}}\int_{-\infty}^{\infty}\tilde{a}(t)e^{i\omega t}dt$], the transmission and reflection coefficients are found to be given respectively by

$$T[\omega] = \frac{\tilde{d}_2[\omega]}{\tilde{d}_1[\omega]} = 1 + \frac{c_+}{\omega - \tilde{\omega}_+} + \frac{c_-}{\omega - \tilde{\omega}_-}, \tag{12}$$

$$R[\omega] = \frac{\tilde{d}_3[\omega]}{\tilde{d}_1[\omega]} = \frac{c_+}{\omega - \tilde{\omega}_+} + \frac{c_-}{\omega - \tilde{\omega}_-}, \tag{13}$$

where $\tilde{\omega}_\pm = -i(\gamma_i/2+\Gamma) \pm (\Delta^2-\Gamma^2)^{1/2}$ are the eigenfrequencies of the model system, and $c_\pm$ are the excitation coefficients of the supermodes given by

$$c_\pm = \frac{-\Gamma(i\sqrt{\Delta^2-\Gamma^2} \pm \Gamma)}{\sqrt{\Delta^2-\Gamma^2}}. \tag{14}$$

Next, we consider the evolution of a Gaussian incident pulse $\tilde{d}_1(t) = \sqrt{1/\tau}\exp(-t^2/\tau^2)$ with its Fourier spectrum given by $\tilde{d}_1[\omega] = \sqrt{\tau/2}\exp(-\omega^2\tau^2/4)$. As an example, we consider the reflection amplitude $\tilde{d}_3(t)$, which is given by

$$\tilde{d}_3(t) = \frac{1}{\sqrt{2\pi}}\int_{-\infty}^{\infty}\tilde{d}_1[\omega]R[\omega]e^{-i\omega t}d\omega. \tag{15}$$

If the pulse duration is short enough to validate the condition $1/\tau > \max\{|\tilde{\omega}_\pm|\}$, we can approximately set $\tilde{d}_1[\omega] \approx \tilde{d}_1[0] = \sqrt{\tau/2}$ and take it out of the integral in Eq. (15). Then, the reflection amplitude is analytically expressed as

$$\tilde{d}_3(t) \approx \sqrt{\pi\tau}(c_+e^{-i\tilde{\omega}_+t} + c_-e^{-i\tilde{\omega}_-t}). \tag{16}$$

More generally, the pulse exhibits totally different dynamics in different phases. In the $\mathcal{PT}$-symmetric phase ($\Gamma > \Delta$), the reflection field amplitude given in Eq. (16) can be further expressed as

$$\tilde{d}_3(t) = \frac{\Gamma\sqrt{\pi\tau}}{\sqrt{\Gamma^2-\Delta^2}}[(\Gamma-\sqrt{\Gamma^2-\Delta^2})e^{-\gamma_-t} - (\Gamma+\sqrt{\Gamma^2-\Delta^2})e^{-\gamma_+t}], \tag{17}$$

where $\gamma_\pm = \gamma_i/2+\Gamma \pm (\Gamma^2-\Delta^2)^{1/2}$ are the decay rates of the supermodes. From Eq. (17), it can be found that the reflection signal contains two different decay rates, corresponding to the bright (+) and dark (−) modes formed in the regime of $\mathcal{PT}$-symmetric phase. The amplitude of these two decaying terms are different ($|c_+/c_-| > 1$) in this phase. The reflection signal becomes zero at the time t_c given by

$$t_c = \frac{1}{\sqrt{\Gamma^2-\Delta^2}}\ln[(\Gamma/\Delta)+\sqrt{(\Gamma/\Delta)^2-1}]. \tag{18}$$

When $t < t_c$, the decay is dominated by $e^{-\gamma_+t}$, while the tail of the signal decays like $e^{-\gamma_-t}$ for $t > t_c$.

In the $\mathcal{PT}$-symmetry-broken phase ($\Gamma < \Delta$), Eq. (16) becomes

$$\tilde{d}_3(t) = \frac{2\Gamma\Delta\sqrt{\pi\tau}}{\sqrt{\Delta^2-\Gamma^2}}\sin(\sqrt{\Delta^2-\Gamma^2}t-\phi)e^{-(\gamma_i/2+\Gamma)t}, \tag{19}$$

where $\phi = \tan^{-1}[(\Delta/\Gamma)^2-1]^{1/2}$. In this region, the supermodes exhibit the same decay rate but different resonance frequencies. Additionally, these two modes are always equally excited ($|c_+/c_-| = 1$), which gives rise to the high-contrast beat of the output signal described by Eq. (19). The beat frequency is determined by $2(\Delta^2-\Gamma^2)^{1/2}$, and the oscillation decays exponentially as $\exp[-(\gamma_i/2+\Gamma)t]$.

The numerical results based on Eq. (15) are presented in Fig. 6. It is clear that in the $\mathcal{PT}$-symmetric phase [Fig. 6(a)], the reflection signal (blue shaded area) first decays with the rate of the bright mode (blue dotted curve), and then approaches the evolution of the dark mode (red solid curve) after t_c. In the symmetry-broken phase [Fig. 6(b)], the two supermodes are equally excited (the red and blue curves coincide), and the high contrast beat [with a unit contrast ratio and a period $T = \pi/(\Delta^2-\Gamma^2)^{1/2}$] can be measured.

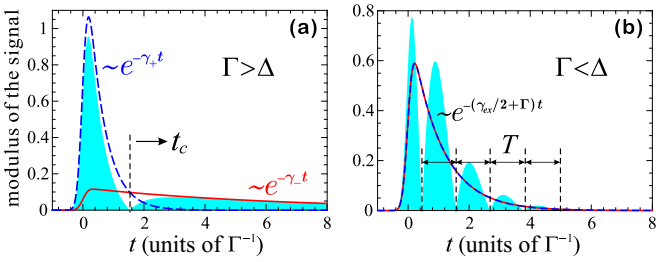

FIG. 6. Evolution of the reflected signal d_3 (blue shaded area) in Config. 2 at (a) $\Gamma/\Delta = 2$ and (b) $\Gamma/\Delta = 1/3$. The red solid curves and blue dashed curves represent the contributions of $\tilde{\omega}_+$ and $\tilde{\omega}_-$, respectively. The results are obtained by numerical integration of Eq. (15) with $\tau = 0.2\Gamma^{-1}$ (0.8 ps).

IV. INFLUENCE OF IMPERFECTIONS IN ACTUAL SYSTEMS

Our proposed schemes can be realized in silicon photonic systems [38] [generalizations of our 2D calculations to three-dimensional (3D) strip waveguides and ring cavities are straightforward]. The required dissipation can be included either by absorption (chemical doping) or radiation loss (using gratings), and the refractive index modulation can be achieved by plasma dispersion [39] or the thermo-optic effect [40]. Here, we consider several common experimental imperfections that can influence the anti-$\mathcal{PT}$ symmetry model we study. We show that the basic features of our model system are robust with respect to small imperfections.

First, we consider the influence of unbalanced loss rates of the modes. In the coupled waveguide system, when the separation distance d_1 between the waveguide a and c differs from the distance d_2 between that of b and c, for instance, caused by fabrication error, the coupling rates κ_1 and κ_2 will become unequal. Consequently, modes a and b would bear different loss rates $\Gamma_1 = |\kappa_1|^2/\gamma$ and $\Gamma_2 = |\kappa_2|^2/\gamma$, respectively. For the cavity configurations discussed later, this kind of imperfections also exist, e.g., the intrinsic loss rates of the two cavities are simply different. The unequal decay rates break the anti-$\mathcal{PT}$ symmetry of the diagonal elements of the Hamiltonian. Taking the waveguide system as an example, the effective Hamiltonian [see Eq. (2)] is then replaced by

$$H = \begin{pmatrix} \Delta - i\Gamma_1 & -i\sqrt{\Gamma_1\Gamma_2} \\ -i\sqrt{\Gamma_1\Gamma_2} & -\Delta - i\Gamma_2 \end{pmatrix}, \tag{20}$$

whose eigenvalues now become [defining $\Gamma = (\Gamma_1+\Gamma_2)/2$]

$$\beta_\pm = -i\Gamma \pm \sqrt{\Delta^2-\Gamma^2-i(\Gamma_1-\Gamma_2)\Delta}. \tag{21}$$

In the ideal case, the mismatch between the eigen-propagation constants, $\Delta\beta = (\beta_+-\beta_-)$ is pure imaginary in the $\mathcal{PT}$-symmetric phase ($\Gamma > \Delta$), real in the broken-symmetry phase ($\Gamma < \Delta$), and vanishes at the EP ($\Gamma = \Delta$). With imperfections, the eigen-propagation constants reduce to $\beta_\pm = -i\Gamma \pm \frac{1-i}{\sqrt{2}}(\Gamma_1^2-\Gamma_2^2)^{1/2}$ at $\Gamma = \Delta$, which suggests that $\Delta\beta$ is composed of equal real and imaginary parts. Although

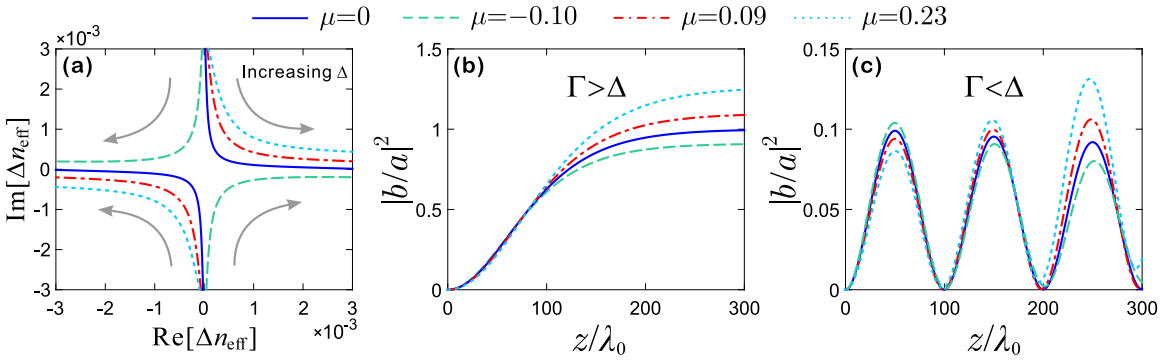

FIG. 7. (a) Evolution of the effective indexes of refraction for the hybrid waveguide system [see Fig. 1(b)] in the complex plane. The different values of $\mu = \{0, -0.10, 0.09, 0.23\}$ result from setting $(d_2 - d_1)/d_1 = \{0, -0.02, 0.02, 0.05\}$, respectively ($d_1$ is fixed to be $0.12\lambda_0$). Δ is increased by increasing the refractive index of waveguide a. Panels (b) and (c) show the correspondingly changed splitting ratio for the two cases considered in Figs. 2(a) and 2(b), respectively.

the eigenmodes do not exactly coalesce, the relaxation rate $|\Delta\beta|$ is still low as long as $|\Gamma_1 - \Gamma_2|$ is sufficiently small. In the vicinity of the EP, the two phases are not well defined because $\Delta\beta$ takes comparable real and imaginary parts. However, deviating from the EP, especially for regions satisfying $|(\Delta^2 - \Gamma^2)/\Delta| \gg |\Gamma_1 - \Gamma_2|$, $\Delta\beta$ exhibits a dominant imaginary part for $\Gamma > \Delta$ and a dominant real part for $\Gamma < \Delta$.

The specific features of the $\mathcal{PT}$-symmetric phase as well as the symmetry-broken phase (e.g., the transport properties) are determined by $\Delta\beta$. When $|\mathrm{Re}(\Delta\beta)/\mathrm{Im}(\Delta\beta)| \ll 1$, the refractionless propagation is preserved because the high-loss mode rapidly decays before it can effectively interfere with the low-loss mode. For $|\mathrm{Re}(\Delta\beta)/\mathrm{Im}(\Delta\beta)| \gg 1$, the oscillation of the mode amplitudes can still be observed because the amplitudes of two modes are comparable within the interference length $|1/|\mathrm{Re}(\Delta\beta)|$. Thus, the basic features of the two phases remain in systems with small imperfections.

The imperfections can influence the size of the avoided crossing $[2(\Gamma_1^2 - \Gamma_2^2)^{1/2}]$ at the EP. In Fig. 7, we show the eigenvalue trajectory and the splitting ratio in the presence of unbalanced decay rates characterized by $\mu = (\Gamma_1 - \Gamma_2)/\Gamma$. As shown in Fig. 7(a), increase of the imperfections causes the eigenvalue trajectories to gradually deviate from the perfect case. The finite $\Delta\beta$ at $\mu = 0$ is due to imperfections of the off-diagonal elements of the Hamiltonian to be discussed below. Figures 7(b) and 7(c) plot the splitting ratio for the cases considered [see Figs. 2(a) and 2(b)] for different values of μ. The basic transport properties are preserved despite imperfections, the small difference being that the splitting ratio converges to a number slightly larger or smaller than unity in the symmetric phase and oscillates with a varying amplitude in the broken-symmetry phase.

Next, we consider the influence of an imperfect anti-Hermitian coupling term. As presented in the Appendix A, the nonvanishing detunings Δk_1 and Δk_2 give rise to a Hermitian component to the coupling Hamiltonian, which also occurs in the first type of cavity Config. 1. For Config. 2, the imperfection arises from the deviation of the optical path $\theta = k_0 n_{\mathrm{eff}} L$ from $2n\pi$. Taking Config. 2 as an example and assuming a small phase deviation $\theta = k_0 n_{\mathrm{eff}} \Delta L$ caused by fabrication error in ΔL, the effective Hamiltonian then changes into

$$H = \begin{pmatrix} \Delta - i\gamma' & -i|\Gamma|e^{i\theta} \\ -i|\Gamma|e^{i\theta} & -\Delta - i\gamma' \end{pmatrix}, \tag{22}$$

with the eigenfrequencies changed to

$$\tilde{\omega}_{\pm} = -i\gamma' \pm \sqrt{\Delta^2 - |\Gamma|^2 e^{i2\theta}}. \tag{23}$$

Similar to the waveguide system discussed above, the characteristics of each phase are determined by the ratio $|\mathrm{Re}(\Delta\omega)/\mathrm{Im}(\Delta\omega)|$, where $\Delta\omega = \omega_+ - \omega_-$ denotes the eigenfrequency mismatch. At the EP, $\Delta\omega$ is approximately given by $2(1-i)\sqrt{2\theta}$, which yields $|\mathrm{Re}(\Delta\omega)/\mathrm{Im}(\Delta\omega)| = 1$. Away from the EP, for regions satisfying $|(\Delta/\Gamma)^2 - 1| \gg \theta$, $|\mathrm{Re}(\Delta\omega)/\mathrm{Im}(\Delta\omega)|$ approaches $|\theta/[(\Delta/\Gamma)^2 - 1]| \ll 1$ for $\Gamma > \Delta$ and approaches $|[(\Delta/\Gamma)^2 - 1]/\theta| \gg 1$ for $\Gamma < \Delta$. Thus, the basic properties of the symmetric and broken-symmetry phase, e.g., the evolution dynamics of an input short pulse discussed in Sec. III, remains observable. Figure 8(a) shows the eigenfrequency trajectories for different phase deviation θ with all other parameters the same as in Fig. 4(d), and Fig. 8(b) plots the ratio $|\mathrm{Re}(\Delta\omega)/\mathrm{Im}(\Delta\omega)|$ versus $|\Gamma/\Delta|$.

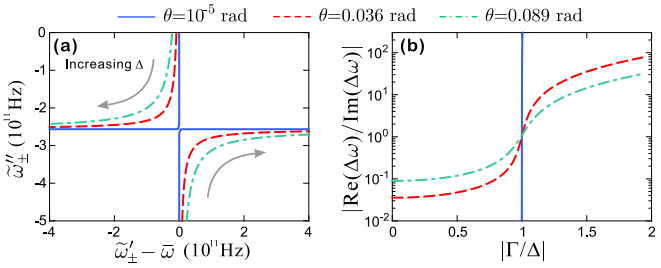

FIG. 8. Influence of the imperfections on the second type resonance structure. (a) Evolution of the eigenfrequencies in the complex plane. (b) The ratio $|\mathrm{Re}(\Delta\omega)/\mathrm{Im}(\Delta\omega)|$ versus $|\Gamma/\Delta|$. The parameters are the same as in Fig. 4(d) except that L is changed to be $L + \Delta L$. Two different values of ΔL, $0.002a_0$ and $0.005a_0$, are considered, respectively corresponding to $\theta = 0.036$ rad and 0.089 rad, and are compared with the case of an ultrasmall θ of 10^{-5} rad.

We find that the sharpness of the ratio around the EP decreases rapidly as $|\theta|$ increases. For actual experimental implementations, current silicon-based fabrication technology can reduce the fabrication error ΔL to several nanometers, which is sufficient for observing the interesting features we predict in the two phases.

V. CONCLUSION

We show that anti-$\mathcal{PT}$ symmetry can be implemented by using dissipative couplings in linear optical systems. The existence of such a symmetry can induce a spontaneous phase transition for the photonic eigenmodes. We illustrate several interesting features endowed by the constant refraction in the $\mathcal{PT}$-symmetric phase, such as a flat broadband mode filtering and dispersion induced dissipation. Further explorations can address interesting behavior of amplification and lasing when suitable gain mechanisms are introduced.

ACKNOWLEDGMENTS

This work is supported by the MOST 2013CB922004 of the National Key Basic Research Program of China and by NSFC (Grants No. 11374176, No. 91421305, No. 11654001, No. 11674390, and No. 91736106). F. Yang acknowledges helpful discussions with Prof. X. S. Jiang of Nanjing University and F. H. Yang of Peking University.

APPENDIX A: ADIABATIC ELIMINATION

In the coupled waveguide system [see Fig. 1(a) in the main text] and the Config. 1 coupled cavity system [see Fig. 4(a) in the main text], the dissipative coupling originates from the adiabatic elimination of the auxiliary lossy mode. The detailed derivation is provided below.

We use the coupled waveguide system shown in Fig. 1(a) as an example. With the coupled-mode theory, the equations of motion for the model read

$$\frac{da}{dz} = -ik_a' a - i\kappa_1 c, \tag{A1}$$

$$\frac{db}{dz} = -ik_b' b - i\kappa_2 c, \tag{A2}$$

$$\frac{dc}{dz} = -ik_c' c - \gamma c - i\kappa_1^* a - i\kappa_2^* b, \tag{A3}$$

where $k_m' = k_m + \kappa_{mm}$ ($\kappa_{mm} = \frac{1}{4}\iint \Delta\epsilon_m |\mathbf{E}_m|^2 dxdy$, $m = a$, b, c) is the modified propagation constant of the mode m, $\kappa_{1/2} = \frac{1}{4}\iint \Delta\epsilon_c \mathbf{E}_{a/b}^* \cdot \mathbf{E}_c dxdy$ is the coupling coefficient of mode a/b with mode c, and γ is the decay constant of the auxiliary lossy mode c. The transversal field of each mode is normalized as $\frac{k_m}{2k_0^2}\iint |\mathbf{E}_m|^2 dxdy = 1$. The equations for the slowly varying amplitudes $\tilde{a}$, $\tilde{b}$, $\tilde{c}$ are then given by

$$\frac{d\tilde{a}}{dz} = -i\kappa_1 \tilde{c} e^{i\Delta k_1 z}, \tag{A4}$$

$$\frac{d\tilde{b}}{dz} = -i\kappa_2 \tilde{c} e^{i\Delta k_2 z}, \tag{A5}$$

$$\frac{d\tilde{c}}{dz} = -\gamma\tilde{c} - i\kappa_1^* \tilde{a} e^{-i\Delta k_1 z} - i\kappa_2^* \tilde{b} e^{-i\Delta k_2 z}, \tag{A6}$$

where $\Delta k_1 = k_a' - k_c'$, and $\Delta k_2 = k_b' - k_c'$. The solution of Eq. (A6) can be formally expressed as

$$\tilde{c}(z) = -i\kappa_1^* \int_0^z dz' \tilde{a}(z') e^{-i\Delta k_1 z'} e^{-\gamma(z-z')} - i\kappa_2^* \int_0^z dz' \tilde{b}(z') e^{-i\Delta k_2 z'} e^{-\gamma(z-z')}, \tag{A7}$$

where the term $\tilde{c}(0)$ at the entrance-associated mode c is taken to be zero. The exponential kernel $e^{-\gamma(z-z')}$ in the integrand will decay to zero as z' deviates significantly from z. Thus, the lower limit of the integral can be chosen as $z - \alpha/\gamma$ if we take $e^{-\alpha} \ll 0$. If the decay rate of mode c is large enough and satisfies $\gamma \gg |\kappa_1|, |\kappa_2|$, then, from Eqs. (A4) and (A5), we know that the changes of mode a and mode b are small within the range α/γ of the integration. Then, we can set $a(z') \approx a(z)$, $b(z') \approx b(z)$, and take them out of the integral in Eq. (A7) to arrive at

$$\begin{aligned}\tilde{c}(z) &\approx -i\kappa_1^* \tilde{a}(z) \int_{z-\alpha/\gamma}^z dz' e^{-i\Delta k_1 z'} e^{-\gamma(z-z')} - i\kappa_2^* \tilde{b}(z) \int_{z-\alpha/\gamma}^z dz' e^{-i\Delta k_2 z'} e^{-\gamma(z-z')} \\ &\approx \frac{-i\kappa_1^*}{\gamma - i\Delta k_1} \tilde{a}(z) e^{-i\Delta k_1 z} + \frac{-i\kappa_2^*}{\gamma - i\Delta k_2} \tilde{b}(z) e^{-i\Delta k_2 z}.\end{aligned} \tag{A8}$$

Substituting Eq. (A8) into Eqs. (A4) and (A5), we adiabatically eliminate mode c. The corresponding equations of motion for mode a and b then reduce to

$$\frac{da}{dz} = \left(-ik_a' - \frac{|\kappa_1|^2}{\gamma - i\Delta k_1}\right) a - \frac{\kappa_1 \kappa_2^*}{\gamma - i\Delta k_2} b, \tag{A9}$$

$$\frac{db}{dz} = \left(-ik_b' - \frac{|\kappa_2|^2}{\gamma - i\Delta k_2}\right) b - \frac{\kappa_1^* \kappa_2}{\gamma - i\Delta k_1} a, \tag{A10}$$

which facilitates the construction of the anti-$\mathcal{PT}$-symmetric Hamiltonian if the following conditions are satisfied: $|\kappa_2| \approx |\kappa_1| = |\kappa|$, and $\gamma \gg |\Delta k_{1/2}|$. We then obtain

$$i\frac{d}{dz}\begin{pmatrix} a \\ b \end{pmatrix} = \begin{pmatrix} \bar{k} + \Delta - i\Gamma & -i\Gamma \\ -i\Gamma & \bar{k} - \Delta - i\Gamma \end{pmatrix} \begin{pmatrix} a \\ b \end{pmatrix}, \tag{A11}$$

where $\bar{k} = (k_a' + k_b')/2$, $\Delta = (k_a' - k_b')/2 \approx (k_a - k_b)/2$, and $\Gamma = |\kappa|^2/\gamma$. This gives Eqs. (1) and (2) in the main text.

As discussed above, the condition for adiabatic elimination is $\gamma \gg |\kappa|$. Thus, to check for the validity of this approximation, we introduce an adiabatic parameter $\xi = |\kappa|/\gamma$, and

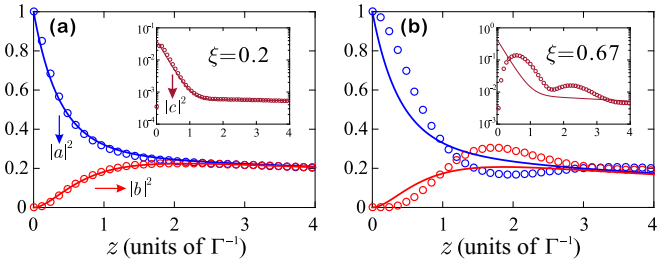

FIG. 9. Comparison between the calculations with (solid curves) and without (circles) adiabatic elimination. Panels (a) and (b) compare different values of ξ at the same ratio of $\Gamma/\Delta = 4$.

compare solutions from solving our model system with and without adiabatic elimination.

The numerical results are presented in Fig. 9. The circles are obtained by solving the rigorous coupled-mode equations [Eqs. (A1)–(A3)], while the solid lines are obtained with adiabatic elimination [Eqs. (A9) and (A10)]. From Fig. 9(a), we find, as expected, that when ξ is small enough ($\xi < 0.2$), the adiabatic elimination represents a good approximation. When ξ becomes larger [Fig. 9(b)], the evolution of the lossy mode c does not quite follow the instantaneous states of a and b, and the adiabatic elimination becomes less accurate.

APPENDIX B: STRUCTURE PARAMETERS OF CAVITY CONFIGURATIONS

The calculations for the optical cavity realization section are based on the 2D structures shown in the inset of Figs. 4(c) and 4(d) in the main text. These structures are designed to achieve resonance at telecommunication wavelengths. For Config. 1, the inner radius R and the width w of the cavity a and c are $R = 0.377a_0$ and $w = 0.140a_0$ ($a_0 = 1.55$ μm), respectively. The width of the waveguide is designed to be the same as the cavity for both configurations. Cavity b has a smaller inner radius of $R' = R - 3 \times 10^{-4}w$, which can be used for fine detuning. The distance is $0.280a_0$ between the waveguide and the cavity, $0.380a_0$ between the cavity a (b) and cavity c, and $1.502a_0$ between the cavity a and b. The imaginary refractive index of the modulated region changes from 0.031 to 0.06 to gradually increase the loss rate of cavity c. In the case of Config. 2, the inner radius and the width of cavity a are the same as those of Config. 1. The distance is $0.140a_0$ between the cavity and the waveguide, and is $L = 2.477a_0$ (which makes $\theta = 14\pi$ around the 1.55 μm telecom wavelength) between the centers of the two cavities. The inner radius of cavity b is changed (from R to $R - 0.005w$) to increase the detuning Δ (from zero to 1.413Γ).

[1] C. M. Bender and S. Boettcher, Phys. Rev. Lett. **80**, 5243 (1998).
[2] C. M. Bender, Rep. Prog. Phys. **70**, 947 (2007).
[3] E. M. Graefe, H. J. Korsch, and A. E. Niederle, Phys. Rev. Lett. **101**, 150408 (2008).
[4] G. L. Celardo and L. Kaplan, Phys. Rev. B **79**, 155108 (2009).
[5] I. Rotter, J. Phys. A: Math. Theor. **42**, 153001 (2009).
[6] V. V. Konotop, J. Yang, and D. A. Zezyulin, Rev. Mod. Phys. **88**, 035002 (2016).
[7] A. Guo, G. J. Salamo, D. Duchesne, R. Morandotti, M. Volatier-Ravat, V. Aimez, G. A. Siviloglou, and D. N. Christodoulides, Phys. Rev. Lett. **103**, 093902 (2009).
[8] C. E. Rüter, K. G. Makris, R. El-Ganainy, D. N. Christodoulides, M. Segev, and D. Kip, Nat. Phys. **6**, 192 (2010).
[9] S. Longhi, Phys. Rev. A **82**, 031801 (2010).
[10] Y. D. Chong, L. Ge, and A. D. Stone, Phys. Rev. Lett. **106**, 093902 (2011).
[11] L. Feng, M. Ayache, J. Huang, Y.-L. Xu, M.-H. Lu, Y.-F. Chen, Y. Fainman, and A. Scherer, Science **333**, 729 (2011).
[12] M. Liertzer, L. Ge, A. Cerjan, A. D. Stone, H. E. Türeci, and S. Rotter, Phys. Rev. Lett. **108**, 173901 (2012).
[13] A. Regensburger, C. Bersch, M.-A. Miri, G. Onishchukov, D. N. Christodoulides, and U. Peschel, Nature (London) **488**, 167 (2012).
[14] N. M. Chtchelkatchev, A. A. Golubov, T. I. Baturina, and V. M. Vinokur, Phys. Rev. Lett. **109**, 150405 (2012).
[15] B. Peng, S. K. Ozdemir, F. Lei, F. Monifi, M. Gianfreda, G. L. Long, S. Fan, F. Nori, C. M. Bender, and L. Yang, Nat. Phys. **10**, 394 (2014).
[16] L. Chang, X. Jiang, S. Hua, C. Yang, J. Wen, L. Jiang, G. Li, G. Wang, and M. Xiao, Nat. Photon. **8**, 524 (2014).
[17] L. Feng, Z. J. Wong, R.-M. Ma, Y. Wang, and X. Zhang, Science **346**, 972 (2014).
[18] J.-Y. Lien, Y.-N. Chen, N. Ishida, H.-B. Chen, C.-C. Hwang, and F. Nori, Phys. Rev. B **91**, 024511 (2015).
[19] A. Cerjan, A. Raman, and S. Fan, Phys. Rev. Lett. **116**, 203902 (2016).
[20] Z.-P. Liu, J. Zhang, K. Özdemir, B. Peng, H. Jing, X.-Y. Lü, C.-W. Li, L. Yang, F. Nori, and Y.-x. Liu, Phys. Rev. Lett. **117**, 110802 (2016).
[21] V. Yannopapas, New J. Phys. **14**, 113017 (2012).
[22] V. Yannopapas, Phys. Rev. A **89**, 013808 (2014).
[23] L. Ge and H. E. Türeci, Phys. Rev. A **88**, 053810 (2013).
[24] J.-H. Wu, M. Artoni, and G. C. La Rocca, Phys. Rev. Lett. **113**, 123004 (2014).
[25] D. A. Antonosyan, A. S. Solntsev, and A. A. Sukhorukov, Opt. Lett. **40**, 4575 (2015).
[26] P. Peng, W. Cao, C. Shen, W. Qu, J. Wen, L. Jiang, and Y. Xiao, Nat. Phys. **12**, 1139 (2016).
[27] K. Fang, Z. Yu, and S. Fan, Phys. Rev. Lett. **108**, 153901 (2012).
[28] A. Yariv and P. Yeh, *Photonics: Optical Electronics in Modern Communications* (Oxford University Press, 2007).
[29] J. Leuthold, R. Hess, J. Eckner, P. Besse, and H. Melchior, Opt. Lett. **21**, 836 (1996).
[30] Y.-F. Xiao, M. Li, Y.-C. Liu, Y. Li, X. Sun, and Q. Gong, Phys. Rev. A **82**, 065804 (2010).
[31] B. Peng, Özdemir, S. Rotter, H. Yilmaz, M. Liertzer, F. Monifi, C. Bender, F. Nori, and L. Yang, Science **346**, 328 (2014).
[32] Y.-C. Liu, Y.-F. Xiao, X. Luan, and C. W. Wong, Phys. Rev. Lett. **110**, 153606 (2013).
[33] L. Maleki, A. Matsko, A. Savchenkov, and V. Ilchenko, Opt. Lett. **29**, 626 (2004).
[34] Q. Xu, S. Sandhu, M. L. Povinelli, J. Shakya, S. Fan, and M. Lipson, Phys. Rev. Lett. **96**, 123901 (2006).
[35] Q. Xu, P. Dong, and M. Lipson, Nat. Phys. **3**, 406 (2007).
[36] Y.-C. Liu, B.-B. Li, and Y.-F. Xiao, Nanophotonics **6**, 789 (2017).
[37] C. W. Gardiner and P. Zoller, *Quantum Noise* (Springer, Berlin, 2004).
[38] D. J. Lockwood and L. Pavesi, *Silicon Photonics II* (Springer, Berlin, 2011).
[39] R. Soref and B. Bennett, IEEE J. Quantum Electron. **23**, 123 (1987).
[40] G. Cocorullo and I. Rendina, Electron. Lett. **28**, 83 (1992).